AGU
ADVANCING EARTH AND SPACE SCIENCE

Geophysical Research Letters

Key Points:
- V_p/V_s ratio obtained by seismic tomography from OBS data is a sensitive tool to constrain lithologies in oceanic basins
- Low V_p/V_s ratios in the South China Sea rule out the occurrence of a wide continent-ocean transition zone of exhumed mantle
- A magmatic-affected continent-ocean transition zone transferring to a thin oceanic domain was revealed

Supporting Information:

Supporting Information may be found in the online version of this article.

Correspondence to:

Y. Li and H. Huang,
liyuhan@scsio.ac.cn;
go223@scsio.ac.cn

Seismic Constraint From V_p/V_s Ratios on the Structure and Composition Across the Continent-Ocean Transition Zone, South China Sea

Yuhan Li[1,2,3] , **Ingo Grevemeyer[2]** , **Haibo Huang[1,4]** , **Xuelin Qiu[1,3,4]** , and **Ziying Xu[4,5]**

[1]Key Laboratory of Ocean and Marginal Sea Geology, South China Sea Institute of Oceanology, Chinese Academy of Sciences, Guangzhou, China, [2]GEOMAR Helmholtz Centre for Ocean Research, Kiel, Germany, [3]University of Chinese Academy of Sciences, Beijing, China, [4]Southern Marine Science and Engineering Guangdong Laboratory (Guangzhou), Guangzhou, China, [5]Key Laboratory of Marine Mineral Resources, Ministry of Natural Resources, Guangzhou Marine Geological Survey, Guangzhou, China

Abstract At non-volcanic passive continental margins, seismic techniques often failed to uniquely define the nature of crustal domains. Here, we overcome this problem by studying the structure and composition of the continent-ocean transition (COT) in the Southwest Sub-basin of the South China Sea, using P and S wave seismic tomography and V_p/V_s ratios, providing unique constraints on lithology. Throughout the image domain, we can rule out large areas of exhumed mantle as V_p/V_s ratios are always <1.9 in the shallow basement layer. Instead, the COT is characterized by extended and fragmented continental crust, and possibly mafic aggregation at the bottom of the crust. In concert with observations from multichannel seismic reflection data, seismic velocities and V_p/V_s ratios suggest that the oldest oceanic crust was formed by starved magmatism, causing rugged basement, thin crust, nearly absent lower crust, and moderately serpentinized mantle below. Our results reveal that rifting occurred without un-roofing continental mantle.

Plain Language Summary Traditional P wave velocity is not able to reveal the detailed rock types in the crust or lithosphere, which are crucial for analyzing the structures and geodynamics in non-volcanic continental margins. In this study, we choose the South China Sea as a case study area, using an effective method to image the V_p/V_s ratio, unraveling the rock type distribution of basalt, gabbro/diabase, serpentinized peridotite in our model from top to bottom. We analyzed the variation of the crustal nature and composition from the continent-ocean transition zone (COT) to the oceanic basin, revealing that the COT is characterized by magmatic intruded continental crust, while the oldest oceanic domain shows a thin oceanic crust overlying mantle that experienced hydration. Our study provides an integrated seismic study which may become a paradigmatic case study to investigate the blurred area of the COT.

1. Introduction

At passive non-volcanic rifted continental margins, the interrelation between rifting, un-roofing of continental mantle in a broad continent-ocean transition zone (COT), and the onset of seafloor spreading is even after decades of geological and geophysical investigations still poorly understood (e.g., Sun et al., 2018). Deep drilling at two non-volcanic margins revealed that at the Iberia-Newfoundland margin the COT is characterized by a wide domain of exhumed mantle (Dean et al., 2000; Whitmarsh et al., 2001), while the mid-northern South China Sea (SCS) margin shows fast break-up without mantle exhumation (Larsen et al., 2018). However, without deep drilling and hence sampling the type of basement rocks, constraints from geophysical imaging alone, are usually too tenuous to uniquely outline the detailed crustal structure forming the seafloor. In seismic exploration, multi-channel seismic data (MCS) provide exquisite basement geometry and shallow crustal characteristics (e.g., Dean et al., 2015; Minshull et al., 2014), while the P wave velocity structure derived from seismic refraction and wide-angle data helps to define the crustal nature (e.g., Dean et al., 2000). However, these traditional approaches are inadequate to reveal the enigmatic structure and composition of the COT. For example, serpentinization of exhumed mantle can hardly be unscrambled from crustal rocks since the P wave velocity overlap at ~6.5–7.2 km/s of gabbro and partially serpentinized peridotite (Christensen, 2004; Grevemeyer, Hayman, et al., 2018). Further, reflection energy

might be weak or absent either at the front of serpentinization or in the vicinity of a poorly defined Moho at the base of oceanic crust and thus can hardly give support to classify different domains. Hence, whether basement is formed by mantle that was exhumed or by seafloor spreading cannot be judged in any case based on *P* wave velocity structure alone.

In a series of laboratory experiments (e.g., Carlson & Miller, 1997; Christensen, 1996, 2004) and in situ case studies (e.g., Grevemeyer, Hayman, et al., 2018; Grevemeyer, Ranero, et al., 2018; Kodaira et al., 1996), a reliable relationship between rock composition and V_p/V_s ratio was established, revealing that V_p/V_s ratio is a sensitive indicator in defining lithologies. Yet, the resolution of the *S* wave model is generally still a challenge when studying V_p/V_s ratios (Holbrook et al., 1992). Forward modeling is generally applied in most studies analyzing V_p/V_s ratios (e.g., Kodaira et al., 1996). However, forward modeling provides often a rather limited depth resolution of Poisson's or V_p/V_s ratio, and is generally preconditioned by the geometry of an existing *P* wave model. In contrast, detailed and independent tomographic inversion of both *P* and *S* wave velocity exhibits excellent abilities to reveal V_p/V_s ratios and associated uncertainties (e.g., Grevemeyer, Hayman, et al., 2018). Generally, a rather thick sedimentary layer blankets the passive margin and incipient oceanic domain, facilitating waveform conversion, but impeding the *S* wave tomographic inversion as conversion may cause asymmetric ray paths for the down-going and up-going wavefield.

At the SCS passive margin, the role of magmatism in the processes of rifting and seafloor spreading is still a matter of debate. MCS and OBS data were used to infer a mantle exhumation model for the COT (Franke et al., 2014; Wan et al., 2019), while the IODP drilling results yielded a rapid transition from continental crust to seafloor spreading and characterized it as an intermediate-type rifted margin (Larsen et al., 2018). Spatial and temporal variations of the magmatic budget in the SCS basin (Yu et al., 2018, 2021) demonstrated the unstable magmatic supply, especially before and after the ridge jump events, leading the architecture of COT in the SCS becomes an open problem and need more evidence. As the thick sediments also are the barrier of rock sampling, the lithology constraint from *S* wave and hence V_p/V_s studies are promising for investigating COT conveniently and economically.

In this study, we introduce a static correction of *S* wave arrivals to nurture *S* wave tomography and applied for the first time an independent tomography of *P* and *S* wave to a non-volcanic margin, the continental margin of the Southwest Sub-basin (SWSB) in the SCS, providing a more robust and elaborate V_p/V_s ratio model. Combined with the analysis of MCS data, we revealed the structure and compositional nature of the COT, making the interpretation of magmatic condition and serpentinization precise. Our study area is located at the northeast rim of SWSB (Figure 1), containing information on rift dynamics and transition from a rifted margin to seafloor spreading. As the oldest part of SWSB, this crucial area also provides an ideal natural laboratory to study the transition period between the first and second stages of seafloor spreading.

2. Tectonic Setting

Since the late Mesozoic, the SCS continental margin experienced extension, causing final break-up and seafloor spreading from ~33 to ~15 Ma (C. Li et al., 2014). The opening of the oceanic basin can be divided into two stages. In the first stage (~33–25 Ma), the East Sub-basin (ESB) opened with the Northwest Sub-basin in the N-S direction. Later, the spreading center jumped to the south (~25 Ma) and the ESB kept opening in NW-direction to NNW-direction with the southwestward propagating of SWSB until ~15 Ma (Sibuet et al., 2016). Our study area is located at the junction of Zhongsha South Trough with the SWSB, south of the Zhongsha Block (Figure 1), documenting the structure style and magmatic condition during the break-up of the Zhongsha Block and its conjugate margin—the Reed Bank.

3. Data and Method

The seismic refraction and wide-angle data set used in this study were collected by the South China Sea Institute of Oceanology, CAS in 2017 (Figure 1). Detailed experiment parameters, data processing, and *P* wave inversion procedure can be accessed in Text S1. Here, we focus on the SWSB where both *P* and *S* wave arrivals of excellent quality have been sampled, revealing the nature of crust or lithosphere from COT to oceanic domain utilizing V_p/V_s ratios.
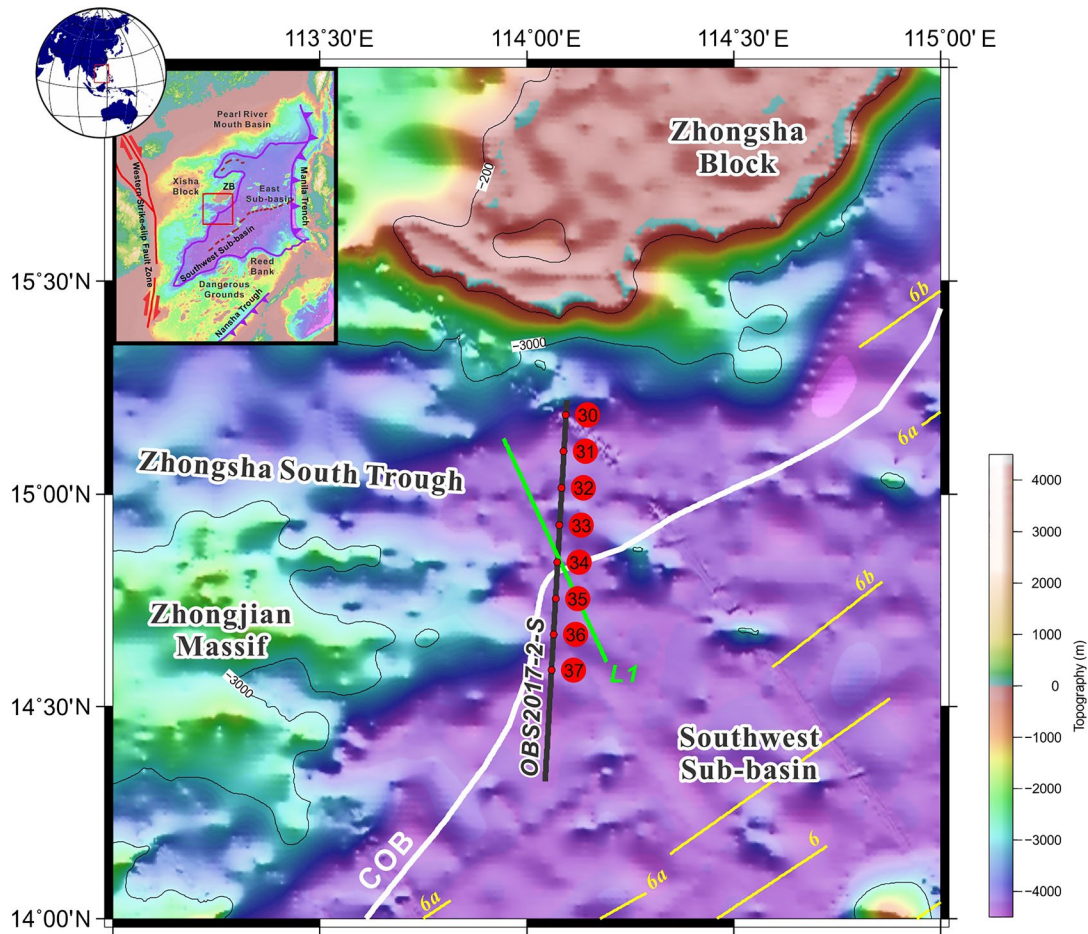
Figure 1. Bathymetry map of the study area, which is extracted from SRTM15_PLUS (Olson et al., 2016). The black and green lines show the location of wide-angle seismic transect OBS2017-2-S and MCS transect L1, respectively. The red dots represent the positions of OBS station. The yellow and white lines show the magnetic lineation (Briais et al., 1993) and continent-ocean boundary (COB), respectively.

Conversion of seismic energy can happen when a seismic ray crosses a sharp boundary between two different elastic/acoustic media (e.g., seafloor and/or basement interface). Therefore, besides the transmission of P wave energy, an S wave is generated and transmitted. In our data set, converted S waves can readily be identified as clear secondary arrivals with relatively slow apparent velocity. Interestingly, the PSS-waves in horizontal components are stronger than the PSP-waves in vertical or hydrophone components (Figures S10–S17). For PSP-waves, the energy runs as a P wave both downward and upward through water and sedimentary blanket, and as an S wave when it turns through crust and mantle (Figure S18). In contrast, PSS is running on its downward path as a P wave through sediment and thereafter as an S wave and therefore downward and upward paths are asymmetric and cannot be utilized directly in our tomographic inversion. PPS-waves run as S wave upward through sedimentary blanket, but elsewhere as a P wave. To benefit from all converted S waves, we picked all of the PSS phases in the horizontal component of the OBS records, and applied a static correction to make the arrival times consistent with those of PSP arrivals (Figures S10–S17), introducing a common datum of conversion. The conversion from PSS-waves to PSP-waves concerns the P and S wave travel-time difference in the sediments beneath the instrument, following the relationship: $T_{PPS} - T_P = T_{PSS} - T_{PSP}$ (Figures S10 and S18). This exercise is necessary as the tomographic code cannot handle conversion itself. Thus, our tomographic model for converted S waves will assume P wave speed in the water and sediments and S wave speed in crust and mantle.

Seismic tomographic inversion software Tomo2D (Korenaga et al., 2000) was used to obtain the P and S wave velocity structure. Throughout the S wave inversion, a heavy damp value was set in the sediment layer to keep the P wave velocity fixed so that the S wave velocity field beneath the basement could be measured
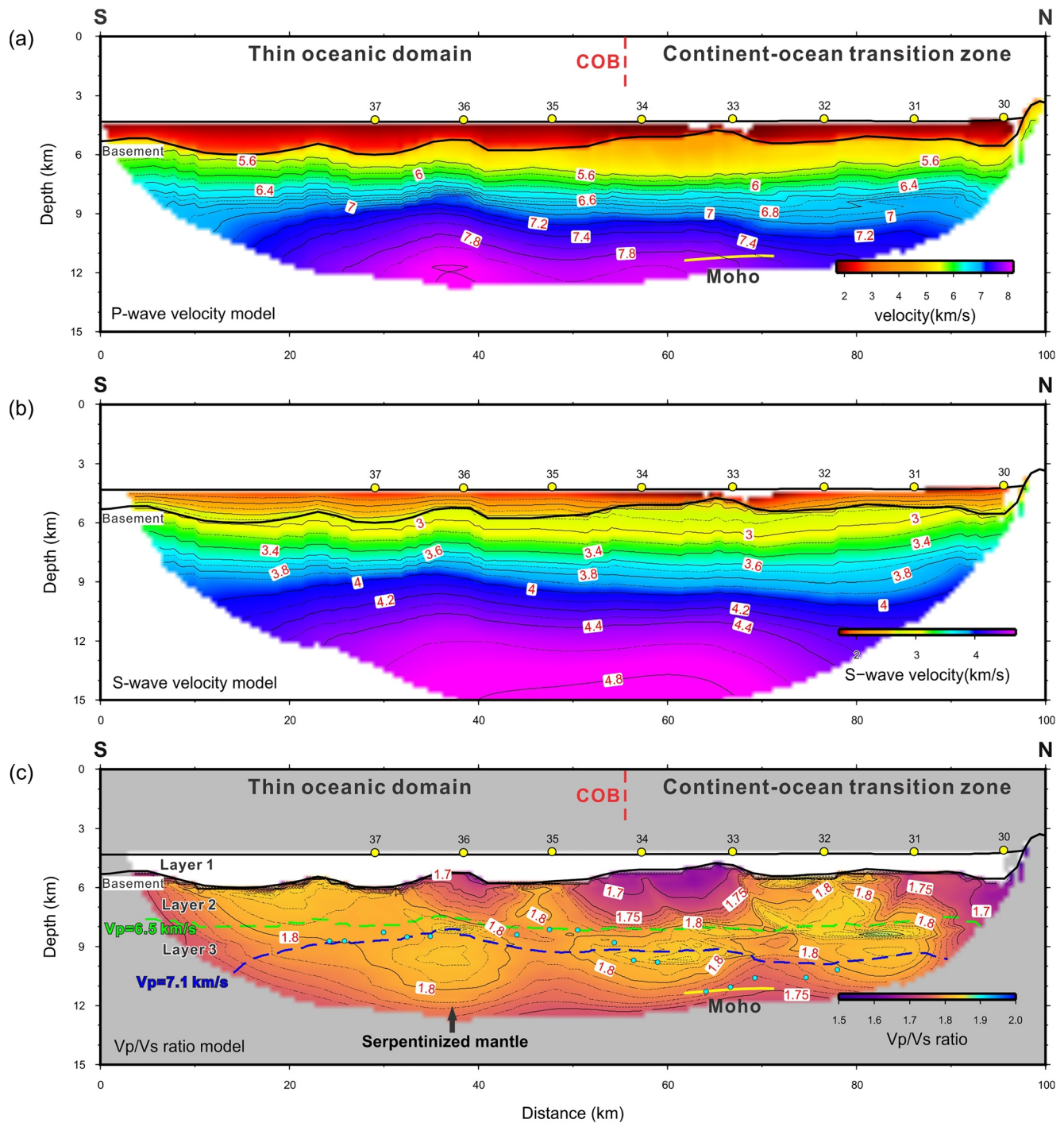
Figure 2. (a) *P* wave velocity, (b) *S* wave velocity, and (c) V_p/V_s ratio model. The yellow line represents the Moho reflector obtained from inversion. The cyan dots represent the projection position of the Moho reflectors from L1 (see Figure 3). Note: the velocities in the sedimentary layer of the *S* wave model represent the values of *P* wave velocity.

accurately by (corrected) PSP phases. V_p/V_s ratios were calculated for the crust and mantle after we obtained the *P* and *S* wave velocity images (Figure 2).

To evaluate the validity of the results, a nonlinear Monte-Carlo error analysis was used to derive model uncertainties. We set 100 1D randomly perturbing initial models for both *P* and *S* wave, and calculated the corresponding reference models. The uncertainties of the model could be measured by the mean deviation
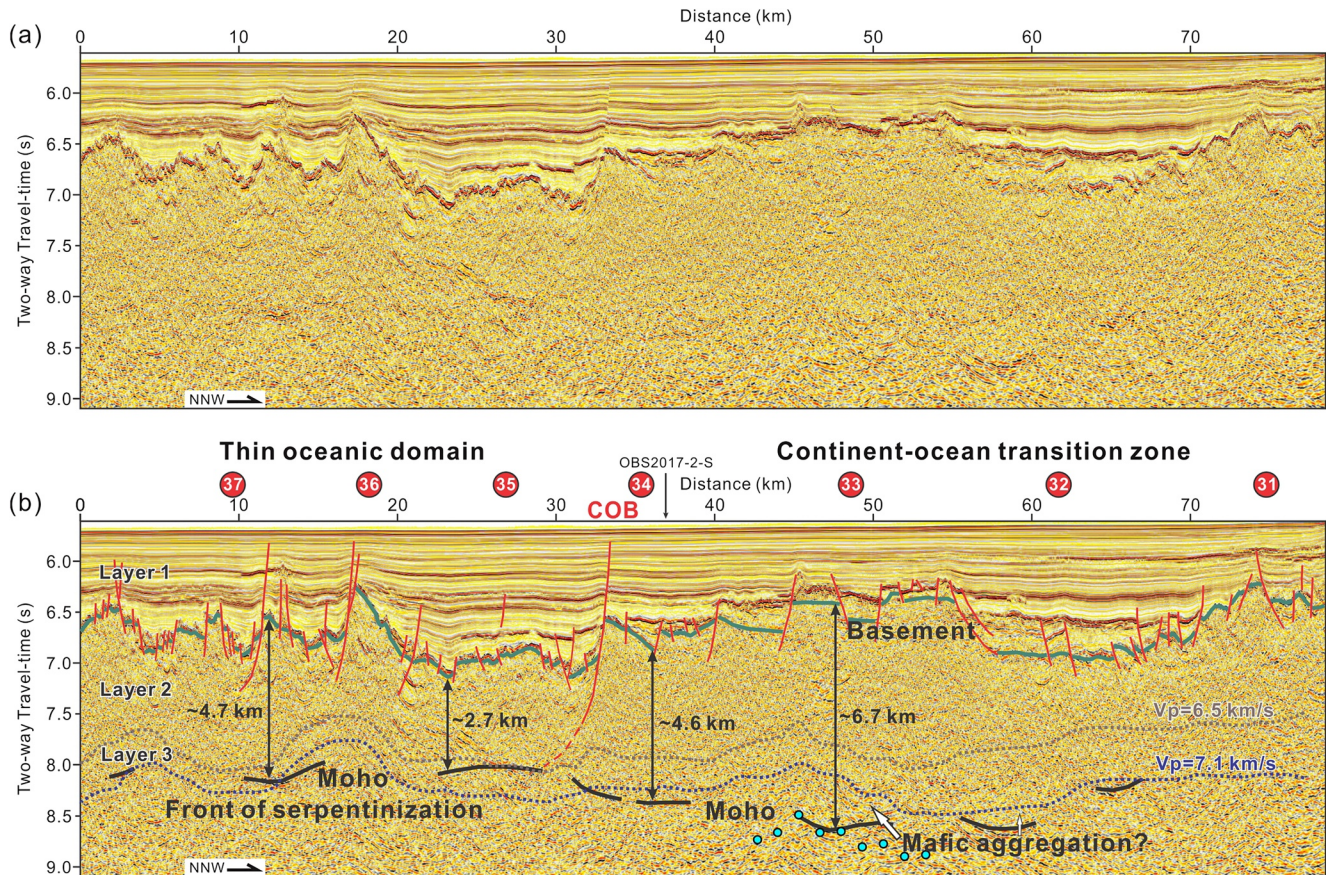
Figure 3. Multichannel seismic profile L1. See Figure 1 for location. The red balls mark the projection of OBS stations from OBS2017-2-S. The dashed brown and blue lines denote the projection of the *P* wave iso-velocity contour of 6.5 and 7.1 km/s, respectively. The cyan dots mark the projection of the Moho reflector from OBS data.

of all solutions (Figure S19). Also, to obtain the uncertainty in the V_p/V_s ratio, we combined 100 different *P* and *S* wave models randomly and calculated its RMS misfit.

In addition, MCS profile L1 (Figure 1) trending NNW-SSE was interpreted to investigate the detailed basement structure and Moho reflectors underneath (Figure 3).

4. Results and Interpretation

One of the key features from the tomographic inversion is that the *P* wave velocity model does not show the typical feature of the oceanic crust, but rather seismic velocity continuously increasing with depth, while normal oceanic crust would support a layered structure. Further, only a short Moho wide-angle reflection turning at ~11.6 km depth was observed beneath OBS33 (Figure 2), but the remaining OBS did not support strong wide-angle reflections. The *P* wave velocity increased from ~4.5 to 5.4 km/s at the top of the basement to 7 km/s at depth of ~8–9.5 km. High velocities of 7.8 km/s characterize the bottom of the model, which occur at shallower depth beneath the southern part of the model when compared to the northern domain with the wide-angle Moho. In the northern part (model distance of >55 km), the crustal velocity structure shows a steep velocity gradient at the base of the crust. Lacking clear characteristics of either continental crust or oceanic crust, the nature of the crust is unclear and we therefore define the northern part as COT (Figures 2 and S20). In the southern part (model distance of <55 km), the velocity gradient becomes extremely steep beneath the 6.4 km/s contour, which we tend to interpret as the existence of serpentinized mantle (Figures 2 and S20).
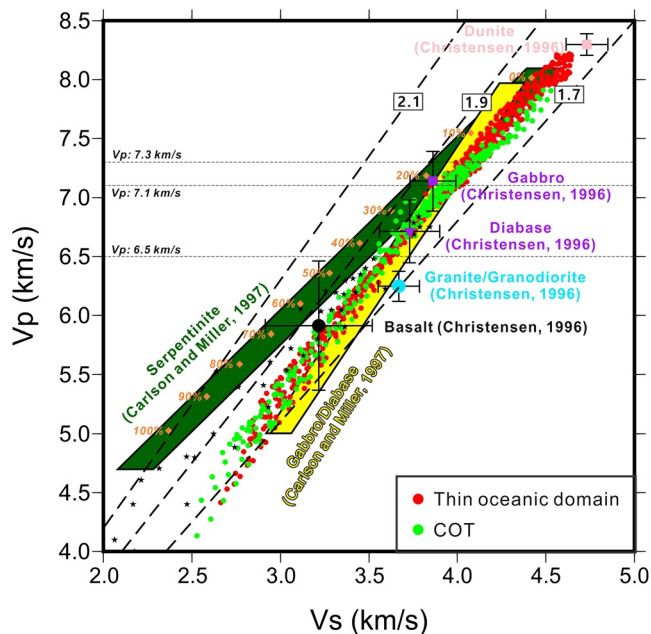
Figure 4. V_p/V_s ratio as a proxy in the SWSB of SCS. The numbers in each panel mark the V_p/V_s ratio. The laboratory velocity ranges of serpentinite and gabbro/diabase (Carlson & Miller, 1997) are showing by the green and yellow areas, respectively. The black circle, light blue circle, purple inverted triangle, purple square, pink square with the error bar marks the velocity range of basalt, granite/granodiorite, diabase, gabbro, and dunite, respectively (Christensen, 1996). The orange diamonds mark the serpentinization degrees (Carlson, 2001). The black five-pointed stars represent the velocity measurement of basalts compiled by Bullock and Minshull (2005). All the laboratory data were measured under a confining pressure of 200 MPa.

In the *S* wave velocity model, the velocities at the top of the crust are ~2.5–3.0 km/s and increase gradually to 3.4 km/s at a depth of ~7 km (Figure 2b). Overall, the *S* wave model mimics the pattern of the *P* wave model, but does not show any well-defined SmS Moho reflection and seismic structure is best characterized as a domain of crustal rocks overlying a gradual crust/mantle transition zone. At ~11 km depth, the velocities reach ~4.4 km/s and increase slowly to >4.8 km/s at the bottom of the model. The uncertainty result shows that the model presents standard deviations <0.075 km/s in most of the area, indicating a satisfactory control of *S* wave velocities (Figure S19b). Only at the top of the crust in areas without any reversed arrivals occur higher uncertainties (±0.1 to ±0.15 km/s).

The V_p/V_s ratio model does not show any distinctive layered structure (Figure 2c). The top of the upper crust shows a large variation of V_p/V_s ratios with the lowest values of <1.75 between OBS33 and OBS35, but elsewhere ratios range from ~1.75 to 1.85. Beneath a depth of 8 km, V_p/V_s ratios are mostly in the range of ~1.75–1.83, showing gently declining values with depth. The uncertainties of V_p/V_s ratios indicate that the result is not very unique within the first 1 km beneath the basement, where uncertainties reach values of ~0.05–0.1 (Figure S19c). Yet, V_p/V_s ratios become less variable with increasing depth, showing uncertainties of <0.05.

In the area with a *P* wave velocity of 6.5–7.1 km/s in our model, the distribution of V_p/V_s ratio is consistent with gabbro or diabase at the pressure of 200 MPa as assessed by Carlson and Miller (1997) and hence support oceanic lower crust (Figure 4). Unfortunately, wide-angle seismic data do not show a well-defined Moho reflection along most of the profile. We therefore define the base of crustal material by the 7.1 km/s iso-velocity contours and the top of layer 3 by the 6.5 km/s iso-velocity contours. Based on these constraints, we observe that the thickness of layer 3 decreases from ~2.0 to ~0.6 km from north to south (Figure 2a). Thus, our results support uncharacteristically thin lower crust when compare with the layer 3 of magmatic oceanic crust (~3.2–5.2 km; Grevemeyer, Ranero, et al., 2018) and typical oceanic crust (average of 4.31 km; Christeson et al., 2019), suggesting a starved magma supply during accretion. Above layer 3, in the V_p range from ~5.4 to 6.5 km/s, the V_p/V_s ratios are consistent with the range of values measured under laboratory conditions on basalt at confining pressure of 200 MPa (Figure 4; Christensen, 1996). The V_p/V_s of basalt always displays a considerable degree of scattering (Bullock & Minshull, 2005, and references therein). However, shallower than V_p of ~5.4 km/s, V_p/V_s ratios are generally lower than the range of basalt, particularly between OBS33 and OBS35.

At the base of our model, and hence at the depth where V_p exceeds 7.3 km/s, the observed V_p/V_s ratios seem to deviate from a characteristic gabbro/diabase trend (Carlson & Miller, 1997; Figure 4), showing instead increased values when compared laterally. In the model distance of <60 km, the average V_p/V_s is consistent with the V_p/V_s range of serpentinized peridotites (Carlson & Miller, 1997), while the northern part has a lower ratio at similar V_p, reflecting rather dry mantle conditions.

The MCS profile L1 crosses line OBS2017-2-S near the southern terminus of the Zhongsha South Trough (Figure 1), showing low amplitude reflections at about 1–2 s below the basement, which are interpreted as Moho reflectors (Figure 3). The Moho reflectors from L1 are weak, but support a relatively consistent impedance contrast. We projected both the Moho reflectors and iso-velocity contours 6.5 and 7.1 km/s from the velocity model onto L1, and also projected the Moho reflectors from L1 onto our V_p/V_s ratio model (Figures 2c and 3b). These Moho reflectors occur close to or above the 7.1 km/s iso-velocity contours in the southern part of the model, supporting that the estimation of the front of serpentinized mantle from iso-velocity contours mimics the base of the crust. Farther north, the Moho reflectors occur beneath the

7.1 km/s iso-velocity contours, indicating a thicker crust and probably supporting increased lower crustal velocities (Figure 2c).

5. Discussion

Rifting at non-volcanic margins and formation of oceanic crust at magma starved conditions cause lithosphere that may share common features, like wide-spread mantle exhumation, for example, at the COT of Newfoundland-Iberia margin (Whitmarsh et al., 2001), or along ultraslow spreading centers like the Southwest Indian Ridge (Sauter et al., 2013), or at the Mid-Cayman Spreading Center (Grevemeyer, Hayman, et al., 2018). In this study, we examined the transition of a rifted margin to the onset of seafloor spreading in an area characterized by a low degree of melting. However, our P wave velocity structure and V_p/V_s ratios provide little evidence for mantle exhumation. If any serpentinization occurred, it occurred at greater depth below the V_p iso-velocity contours of ~7.3 km/s in the southern part of the model (Figures 2 and 4) where MCS data provided evidence for the Moho reflections and beneath that, V_p/V_s ratios are with ~1.8 in the range that elsewhere hydrated mantle was deduced (Grevemeyer, Ranero, et al., 2018; Prada et al., 2016). Here, MCS data reveal a rugged and faulted basement (profile distance 0–33 km in Figure 3), which may have provided the pathways for water to migrate into the mantle, leading to hydration below Moho. Based on P wave velocity, the amount of serpentinized peridotite is estimated to be <17% according to the classification of Carlson (2001). Grevemeyer, Hayman, et al. (2018) obtained V_p/V_s ratios at the ultraslow-spreading center Mid-Cayman Ridge, their result revealed large domains with $V_p/V_s > 1.9$ outlining wide-spread mantle serpentinization degree of >70%, suggesting that 25% of the insonified volume of the lithosphere could be classified as serpentinized mantle. In addition, mantle exhumation was revealed in back-arc basins, such as the Magnaghi-Vavilov Basin (Tyrrhenian Sea, Mediterranean) by revealing V_p/V_s ratios of ~1.9 at the shallow depth (Prada et al., 2016). Further, at the Gobar Spur non-volcanic margin, Bullock and Minshull (2005) found seaward of the continental slope a roughly 120 km wide zone of exhumed mantle. At Goban Spur, V_p/V_s ratios were in the order of 1.9–2.0 and hence much larger than anywhere in our insonified volume, supporting dominantly normal crustal rocks and rocks emplaced by magmatic accretion during the initial opening of SWSB, consistent with the IODP results in the mid-northern SCS margin (Larsen et al., 2018).

By approximating the bottom of oceanic crust by the 7.1 km/s iso-velocity contour (Figure 4), the crustal thickness variates from ~2.6 to ~4.5 km in the oceanic domain, which is consistent with the thickness of ~2.7–4.7 km obtained from the MCS data (Figure 3). Interestingly, most of the melt reduction is expressed in the lower crust, revealing that ~78% of crustal thinning occurred in the lower crust (thinned by ~1.4 km), while the thickness of the upper crust keeps almost constant. This observation corresponds to the conclusion of a positive relationship between layer 3 thickness and whole oceanic crustal thickness (e.g., Mutter & Mutter, 1993). The half-spreading rate in the SWSB is ~17.5–25 mm/yr, illustrating a slow-spreading oceanic basin (C. Li et al., 2014). Several case studies and reviews have demonstrated that the crustal thickness (Chen, 1992) and velocities (Grevemeyer, Ranero, et al., 2018) of the slow-spreading crust have a much wider variability than intermediate- and fast-spreading crust. The crustal thickness of oceanic domain deduced from discrimination of lithology in our study mimics the range of slow-spreading crustal thickness compiled by Chen (1992). To the southwest of our line, seismic data revealed a crustal thickness of only ~1.5–3.6 km (Yu et al., 2018), thinner than our result, which may support a gradually decreasing melt supply while spreading propagated southwestward during the opening of SWSB (J. B. Li et al., 2012).

A key feature of the V_p/V_s ratios is the small ratios below OBS33 and OBS35. Laboratory experiments on basaltic rocks suggest that the V_p/V_s ratio will decrease with the decreasing porosity and crack density (Hyndman, 1979). Thus, the low V_p, low V_p/V_s ratio anomaly cannot be explained by high porosity in basalt or volcanoclastic sediments. Further, most open cracks would have been sealed over the past ~25 Ma since break-up (Flovenz, 1980; Gillis & Sapp, 1997). In continental crust, V_p/V_s ratio decreases with increasing content of SiO_2, which is usually lower than 1.75 in felsic rocks (Christensen, 1996). We thus infer that the areas of low V_p/V_s ratios mainly consist of remnant fragments of continental crust embedded in either oceanic crust or represent magmatically intruded continental crust. This may also explain the occurrence of a wide-angle Moho reflection in this domain (Figures 2c and 3b) as Moho is generally better defined

in continental crust than oceanic slow-spreading crust. Further, MCS data show that the basement here consists of relatively large fault-blocks which are characterized by flat horsts and grabens, showing a distinctively different feature than the thin oceanic crustal domain (Figure 3), supporting the definition of the continent-ocean boundary in C. Li et al. (2014).

In contrast to the domain below the thin oceanic crust (V_p/V_s ~1.8), V_p/V_s ratios of ~1.75 in the inferred mantle beneath the COT support a rather dry and normal mantle (Figures 2c and 4). This observation could support the occurrence of mafic rocks with an increasing Mg/Fe ratio (Browning, 1984). We therefore hypothesized that this area has been affected by magnesium-rich mafic aggregates which may have formed during the relatively long time of rifting and at high temperatures while the two rigid blocks attempted to separate (e.g., Christensen, 1996; Kelemen & Holbrook, 1995; White & Smith, 2009). The abundant magmatic supply reflected by this area shows huge contrast with the southern part of our model since the Zhongsha South Trough may be formed and developed in the first stage of seafloor spreading (~33–25 Ma) in N-S spreading direction, similar to the formation of high velocities in the lower crust of northeastern SCS margin. After spreading ridge reorientation (after ~25 Ma), the spreading direction changed to NW-SE (Sibuet et al., 2016) and the magmatic budget may decrease during this process, forming thin oceanic crust in SWSB.

6. Conclusion

We constructed a V_p/V_s ratio model for the COT of the SWSB in the SCS using *P* and *S* wave seismic tomography. With the aid of the V_p/V_s ratios in defining lithologies, and structural images from MCS data, we revealed that V_p/V_s ratios of <1.9 in the shallow basement layer rule out that mantle exhumation occurred during the final stage of rifting and continental break-up. Instead, the COT is characterized by fragments of continental crust. Velocities of >7.1 km/s in the lower crust may support mafic lower crustal intrusions. Adjacent to it, we identify a rather thin oceanic crust (~2.6–4.5 km), supporting a starved magmatic condition with mantle serpentinization underlying during early seafloor spreading.

Data Availability Statement

Supplementary text and figures supporting the conclusions can be found in the Supporting Information. All the OBS seismic data used in this study can be accessed through http://doi.org/10.5281/zenodo.5117845.

References

Briais, A., Patriat, P., & Tapponnier, P. (1993). Updated interpretation of magnetic anomalies and seafloor spreading stages in the South China Sea: Implications for the Tertiary tectonics of Southeast Asia. *Journal of Geophysical Research*, *98*, 6299–6328. https://doi.org/10.1029/92JB02280

Browning, P. (1984). Cryptic variation within the cumulate sequence of the Oman ophiolite: Magma chamber depth and petrological implications. *Geological Society, London, Special Publications*, *13*(1), 71–82. https://doi.org/10.1144/GSL.SP.1984.013.01.07

Bullock, A. D., & Minshull, T. A. (2005). From continental extension to seafloor spreading: Crustal structure of the Goban Spur rifted margin, southwest of the UK. *Geophysical Journal International*, *163*, 527–546. https://doi.org/10.1111/j.1365-246X.2005.02726.x

Carlson, R. L. (2001). The abundance of ultramafic rocks in Atlantic Ocean crust. *Geophysical Journal International*, *144*, 37–48. https://doi.org/10.1046/j.0956-540X.2000.01280.x

Carlson, R. L., & Miller, D. J. (1997). A new assessment of the abundance of serpentinite in the oceanic crust. *Geophysical Research Letters*, *24*(4), 457–460. https://doi.org/10.1029/97GL00144

Chen, Y. J. (1992). Oceanic crustal thickness versus spreading rate. *Geophysical Research Letters*, *19*(8), 753–756. https://doi.org/10.1029/92GL00161

Christensen, N. I. (1996). Poisson's ratio and crustal seismology. *Journal of Geophysical Research*, *101*(B2), 3139–3156. https://doi.org/10.1029/95JB03446

Christensen, N. I. (2004). Serpentinites, peridotites, and seismology. *International Geology Review*, *46*(9), 795–816. https://doi.org/10.2747/0020-6814.46.9.795

Christeson, G. L., Goff, J. A., & Reece, R. S. (2019). Synthesis of oceanic crustal structure from two-dimensional seismic profiles. *Review of Geophysics*, *57*, 504–529. https://doi.org/10.1029/2019RG000641

Dean, S. M., Minshull, T. A., Whitmarsh, R. B., & Louden, K. E. (2000). Deep structure of the ocean-continent transition in the southern Iberia Abyssal Plain from seismic refraction profiles: The IAM-9 transect at 40° 20′N. *Journal of Geophysical Research*, *105*, 5859–5885. https://doi.org/10.1029/1999JB900301

Dean, S. M., Sawyer, D. S., & Morgan, J. K. (2015). Galicia Bank ocean–continent transition zone: New seismic reflection constraints. *Earth and Planetary Science Letters*, *413*, 197–207. https://doi.org/10.1016/j.epsl.2014.12.045

Flovenz, O. G. (1980). Seismic structure of the Icelandic crust above layer three and the relation between body wave velocity and the alteration of the basaltic crust. *Journal of Geophysics*, *47*(1), 211–220.

Franke, D., Savva, D., Pubellier, M., Steuer, S., Mouly, B., Auxietre, J.-L., et al. (2014). The final rifting evolution in the South China Sea. *Marine and Petroleum Geology*, *58*(B), 704–720. https://doi.org/10.1016/j.marpetgeo.2013.11.020

Gillis, K. M., & Sapp, K. (1997). Distribution of porosity in a section of upper oceanic crust exposed in the Troodos Ophiolite. *Journal of Geophysical Research*, *102*(B5), 10133–10149. https://doi.org/10.1029/96JB03909

Grevemeyer, I., Hayman, N. W., Peirce, C., Schwardt, M., Van Avendonk, H. J. A., Dannowski, A., & Papenberg, C. (2018). Episodic magmatism and serpentinized mantle exhumation at an ultraslow-spreading centre. *Nature Geoscience*, *11*, 444–448. https://doi.org/10.1038/s41561-018-0124-6

Grevemeyer, I., Ranero, C. R., & Ivandic, M. (2018). Structure of oceanic crust and serpentinization at subduction trenches. *Geosphere*, *14*(2), 395–418. https://doi.org/10.1130/GES01537.1

Holbrook, W. S., Mooney, W. D., & Christensen, N. J. (1992). The seismic velocity structure of the deep continental crust. In D. M. Fountain, R. Arculus, & R. W. Kay (Eds.), Continental lower crust. Development in geotectonics (Vol. 23, pp. 1–43). Elsevier.

Hyndman, R. (1979). Poisson's ratio in the oceanic crust – A review. *Tectonophysics*, *59*(1–4), 321–333. https://doi.org/10.1016/0040-1951(79)90053-2

Kelemen, P. B., & Holbrook, W. S. (1995). Origin of thick, high-velocity igneous crust along the U.S. East Coast Margin. *Journal of Geophysical Research*, *100*(B7), 10077–10094. https://doi.org/10.1029/95JB00924

Kodaira, S., Bellenberg, M., Iwasaki, T., Kanazawa, T., Hirschleber, H. B., & Shimamura, H. (1996). Vp/Vs ratio structure of the Lofoten continental margin, northern Norway, and its geological implications. *Geophysical Journal International*, *124*(3), 724–740. https://doi.org/10.1111/j.1365-246X.1996.tb05634.x

Korenaga, J., Holbrook, W. S., Kent, G. M., Kelemen, P. B., Detrick, R. S., Larsen, H.-C., et al. (2000). Crustal structure of the southeast Greenland margin from joint refraction and reflection seismic tomography. *Journal of Geophysical Research*, *105*(B9), 21591–21614. https://doi.org/10.1029/2000JB900188

Larsen, H. C., Mohn, G., Nirrengarten, M., Sun, Z., Stock, J., Jian, Z., et al. (2018). Rapid transition from continental breakup to igneous oceanic crust in the South China Sea. *Nature Geoscience*, *11*(10), 782–789. https://doi.org/10.1038/s41561-018-0198-1

Li, C., Xu, X., Lin, J., Sun, Z., Zhu, J., Yao, Y., et al. (2014). Ages and magnetic structures of the South China Sea constrained by deep tow magnetic surveys and IODP Expedition 349. *Geochemistry, Geophysics, Geosystems*, *15*, 4958–4983. https://doi.org/10.1002/2014GC005567

Li, J. B., Ding, W. W., Wu, Z. Y., Zhang, J., & Dong, C. Z. (2012). The propagation of seafloor spreading in the southwestern subbasin, South China Sea. *Chinese Science Bulletin*, *57*(24), 3182–3191. https://doi.org/10.1007/s11434-012-5329-2

Minshull, T. A., Dean, S. M., & Whitmarsh, R. B. (2014). The peridotite ridge province in the southern Iberia Abyssal Plain: Seismic constraints revisited. *Journal of Geophysical Research: Solid Earth*, *119*, 1580–1598. https://doi.org/10.1002/2014JB011011

Mutter, C. Z., & Mutter, J. C. (1993). Variations in thickness of layer 3 dominate oceanic crustal structure. *Earth and Planetary Science Letters*, *117*, 295–317. https://doi.org/10.1016/0012-821X(93)90134-U

Olson, C. J., Becker, J. J., & Sandwell, D. T. (2016). *SRTM15_PLUS: Data fusion of Shuttle Radar Topography Mission (SRTM) land topography with measured and estimated seafloor topography* (NCEI Accession 0150537).

Prada, M., Ranero, C. R., Sallarès, V., Zitellini, N., & Grevemeyer, I. (2016). Mantle exhumation and sequence of magmatic events in the Magnaghi–Vavilov Basin (Central Tyrrhenian, Italy): New constraints from geological and geophysical observations. *Tectonophysics*, *689*, 133–142. https://doi.org/10.1016/j.tecto.2016.01.041

Sauter, D., Cannat, M., Roumejon, S., Andreani, M., Birot, D., Bronner, A., et al. (2013). Continuous exhumation of mantle-derived rocks at the Southwest Indian Ridge for 11 million years. *Nature Geoscience*, *6*(4), 314–320. https://doi.org/10.1038/ngeo1771

Sibuet, J.-C., Yeh, Y.-C., & Lee, C.-S. (2016). Geodynamics of the South China Sea. *Tectonophysics*, *692*, 98–119. https://doi.org/10.1016/j.tecto.2016.02.022

Sun, Z., Stock, J., Klaus, A., Klaus, A., & the Expedition 367 Scientists. (2018). *Expedition 367 Preliminary Report: South China Sea Rifted Margin*. International Ocean Discovery Program. https://doi.org/10.14379/iodp.pr.367.2018

Wan, X., Li, C.-F., Zhao, M., He, E., Liu, S., Qiu, X., et al. (2019). Seismic velocity structure of the magnetic quiet zone and continent-ocean boundary in the northeastern South China Sea. *Journal of Geophysical Research: Solid Earth*, *124*, 11866–11899. https://doi.org/10.1029/2019JB017785

Wessel, P., & Smith, W. H. F. (1995). New version of the generic mapping tools released. *Eos, Transactions American Geophysical Union*, *76*, 329. https://doi.org/10.1029/95eo00198

White, R. S., & Smith, L. K. (2009). Crustal structure of the Hatton volcanic rifted continental margin and the conjugate Greenland margin, NE Atlantic. *Journal of Geophysical Research*, *114*, B02305. https://doi.org/10.1029/2008JB005856

Whitmarsh, R. B., Manatschal, G., & Minshull, T. A. (2001). Evolution of magma-poor continental margins from rifting to seafloor spreading. *Nature*, *413*, 150–154. https://doi.org/10.1038/35093085

Yu, J., Yan, P., Qiu, Y., Delescluse, M., Huang, W., & Wang, Y. (2021). Oceanic crustal structures and temporal variations of magmatic budget during seafloor spreading in the East Sub-basin of the South China Sea. *Marine Geology*, *436*, 106475. https://doi.org/10.1016/j.margeo.2021.106475

Yu, J., Yan, P., Wang, Y., Zhang, J., Qiu, Y., Pubellier, M., & Delescluse, M. (2018). Seismic evidence for tectonically dominated seafloor spreading in the Southwest Sub-basin of the South China Sea. *Geochemistry, Geophysics, Geosystems*, *19*, 3459–3477. https://doi.org/10.1029/2018GC007819

References From the Supporting Information

Davy, R. G., Minshull, T. A., Bayrakci, G., Bull, J. M., Klaeschen, D., Papenberg, C., et al. (2016). Continental hyperextension, mantle exhumation, and thin oceanic crust at the continent-ocean transition, West Iberia: New insights from wide-angle seismic. *Journal of Geophysical Research: Solid Earth*, *121*, 3177–3199. https://doi.org/10.1002/2016JB012825

White, R. S., McKenzie, D., & O'Nions, R. K. (1992). Oceanic crustal thickness from seismic measurements and rare Earth element inversions. *Journal of Geophysical Research*, *97*(B13), 19683–19715. https://doi.org/10.1029/92JB01749

Whitmarsh, R. B., White, R. S., Horsefield, S. J., Sibuet, J.-C., Recq, M., & Louvel, V. (1996). The ocean-continent boundary off the western continental margin of Iberia: Crustal structure west of Galicia Bank. *Journal of Geophysical Research*, *101*(B12), 28291–28314. https://doi.org/10.1029/96JB02579